Small-scale open ocean currents have large effects on wind wave heights

Fabrice Ardhuin, Sarah T. Gille, Dimitris Menemenlis, Cesar B. Rocha, Nicolas Rascle, Bertrand Chapron, Jonathan Gula, Jeroen Molemaker

AGU PUBLICATIONS

JGR

Journal of Geophysical Research: Oceans

RESEARCH ARTICLE

10.1002/2016JC012413

Small-scale open ocean currents have large effects on wind wave heights

Fabrice Ardhuin[1], Sarah T. Gille[2], Dimitris Menemenlis[3], Cesar B. Rocha[2], Nicolas Rascle[1], Bertrand Chapron[1], Jonathan Gula[1], and Jeroen Molemaker[1]

[1]Univ. Brest, CNRS, IRD, Ifremer, Laboratoire d'Océanographie Physique et Spatiale (LOPS), IUEM, Brest, France, [2]Scripps Institution of Oceanography, University of California San Diego, La Jolla, California, USA, [3]Jet Propulsion Laboratory, California Institute of Technology, Pasadena, California, USA

Key Points:
- Wave height gradients at scales under 100 km are determined by currents
- The wave height variance at 10 km scale is proportional to the current spectrum
- If not corrected for by measuring gradients in wave parameters, SWOT error on sea level probably exceed 20% of total allowed error

Correspondence to:
F. Ardhuin,
ardhuin@ifremer.fr

Citation:
Ardhuin, F., S. T. Gille, D. Menemenlis, C. B. Rocha, N. Rascle, B. Chapron, J. Gula, and J. Molemaker (2017), Small-scale open ocean currents have large effects on wind wave heights, *J. Geophys. Res. Oceans*, *122*, 4500–4517, doi:10.1002/2016JC012413.

Received 10 OCT 2016
Accepted 9 APR 2017
Accepted article online 13 APR 2017
Published online 1 JUN 2017

Abstract Tidal currents and large-scale oceanic currents are known to modify ocean wave properties, causing extreme sea states that are a hazard to navigation. Recent advances in the understanding and modeling capability of open ocean currents have revealed the ubiquitous presence of eddies, fronts, and filaments at scales 10–100 km. Based on realistic numerical models, we show that these structures can be the main source of variability in significant wave heights at scales less than 200 km, including important variations down to 10 km. Model results are consistent with wave height variations along satellite altimeter tracks, resolved at scales larger than 50 km. The spectrum of significant wave heights is found to be of the order of $70\langle H_s\rangle^2/(g^2\langle T_{m0,-1}\rangle^2)$ times the current spectrum, where $\langle H_s\rangle$ is the spatially averaged significant wave height, $\langle T_{m0,-1}\rangle$ is the energy-averaged period, and g is the gravity acceleration. This variability induced by currents has been largely overlooked in spite of its relevance for extreme wave heights and remote sensing.

Plain Language Summary We show that the variations in currents at scales 10 to 100 km are the main source of variations in wave heights at the same scales. Our work uses a combination of realistic numerical models for currents and waves and data from the Jason-3 and SARAL/AltiKa satellites. This finding will be of interest for the investigation of extreme wave heights, remote sensing, and air-sea interactions. As an immediate application, the present results will help constrain the error budget of the up-coming satellite missions, in particular the Surface Water and Ocean Topography (SWOT) mission, and decide how the data will have to be processed to arrive at accurate sea level and wave measurements. It will also help in the analysis of wave measurements by the CFOSAT satellite.

1. Introduction

The analysis and numerical modeling of ocean currents and waves have historically been developed separately. Yet currents can influence waves, as it is well documented for large-scale currents, particularly the Agulhas current [e.g., *Irvine and Tilley*, 1988] and the Gulf Stream [e.g., *Mapp et al.*, 1985]. Although the same physical principles should apply, the impact of smaller-scale currents has been little explored in the open ocean, with the exception of currents associated with internal waves [e.g., *Osborne and Burch*, 1980].

Knowledge on small-scale ocean flows, including the so-called submesoscales, has only emerged recently. Submesoscales are "structures in the form of density fronts and filaments, topographic wakes, and persistent coherent vortices [. . .] created from mesoscale eddies and strong currents" [*McWilliams*, 2016].

The present paper examines how currents at scales of 10–100 km in the open ocean modify the heights of surface waves. The currents we consider include mesoscale, submesoscales, and internal waves.

Neglecting diffraction and scattering effects, generally not relevant at scales over 1 km, i.e., larger than the wavelength of ocean waves [e.g., *Magne et al.*, 2007; *WISE Group*, 2007], the wavefield represented by the two-dimensional wave action spectrum $N(k,\theta)$ evolves in time and space according to [e.g., *Komen et al.*, 1994],

$$\frac{\partial N}{\partial t}+\frac{\partial}{\partial \lambda}\left(\dot{\lambda}N\right)+\frac{\partial}{\partial \phi}\left(\dot{\phi}N\right)+\frac{\partial}{\partial k}\left(\dot{k}N\right)+\frac{\partial}{\partial \theta}\left(\dot{\theta}N\right)=\frac{S}{\sigma}, \tag{1}$$

where t is time, λ and ϕ are longitude and latitude, k is the wave number magnitude, and θ is the wave propagation direction relative to East (oriented so that eastward propagating waves have $\theta = 0$). On the right-hand side, S is the sum of the energy source terms that represent the interactions with winds, bottom, wave-wave interactions, and dissipation. Division by the intrinsic frequency σ converts the energy source S to a source of action.

For simplicity, we neglect nonlinear wave action advection by the Stokes drift and differential advection of different components due to a vertical shear in the current. Hence, we use the surface values u_E and v_E of the zonal and meridional current components, provided by a circulation model. A more general treatment is given by *Andrews and McIntyre* [1978] or *Kirby and Chen* [1989], which could reduce the current impact in the presence of strong near-surface shear, in particular for large wave periods. For example, a linear shear reducing the current speed from 1 m s^{-1} at the surface to 0 at 20 m depth gives an effective current speed of 0.5 m s^{-1} for a wave period of 10 s ($L = 150$ m) instead of the 1 m s^{-1} surface value.

Propagation speeds in physical and spectral space are given by the following expressions [*Tolman*, 1990]:

$$\dot{\theta}=\dot{\theta}_{DG}+\frac{\sin^2\theta}{R\cos\phi}\frac{\partial v_E}{\partial \lambda}-\frac{\cos^2\theta}{R}\frac{\partial u_E}{\partial \phi}+\frac{\cos\theta\,\sin\theta}{R}\left(\frac{1}{\cos\phi}\frac{\partial u_E}{\partial \lambda}-\frac{\partial v_E}{\partial \phi}\right), \tag{2}$$

$$\dot{\lambda}=\left(C_g\sin\theta+a\,u_E\right)/(R\cos\phi), \tag{3}$$

$$\dot{\phi}=\left(C_g\cos\theta+a\,v_E\right)/R, \tag{4}$$

$$\dot{k}=-\frac{\partial\sigma}{\partial D}\frac{\mathbf{k}}{k}\cdot\nabla D-\mathbf{k}\cdot\nabla\,\boldsymbol{u}_E. \tag{5}$$

Here D is the water depth, $\dot{\theta}_{DG}$ is the apparent wave rotation velocity due to water depth gradients and Earth sphericity, R is the Earth radius, $C_g=\partial\sigma/\partial k$ is the intrinsic group speed given by the linear wave dispersion relation

$$\sigma^2=gk\,\tanh\left(kD\right), \tag{6}$$

and $\omega=\sigma+\mathbf{k}\cdot\boldsymbol{u}_E$ is the absolute frequency. The advection coefficient a is equal to 1, except in specific model tests where we set $a = 0$ to investigate the impact of the advection terms.

The current vector $\mathbf{u}_E$ directly impacts the waves through four mechanisms, each represented by a separate term in equation (1).

1. The refraction term $\dot{\theta}$ in equation (2): the turning of the waves can produce large variations in wave heights in the case of monochromatic waves.
2. The advection of wave action at the speed $\boldsymbol{C}_g+a\mathbf{u}_E$ in equations (3) and (4). It should be noted that C_g also adjusts to the change in current velocity. This advection by the current is deactivated by setting $a = 0$.
3. The change in wave number $\dot{k}$ or "concertina effect" represents a change in wavelength that is also associated with an exchange of energy between waves and currents, and a change in group speed C_g.
4. The source term S is a function of the wind speed relative to the current speed, typically $\mathbf{U}_{10}-r\mathbf{u}_E$ with $r = 0$ when neglecting the current, and $r = 1$ for a full effect of the current, which neglects the adjustment of the atmosphere to the surface current velocity [*Hersbach and Bidlot*, 2008]. That adjustment was found to give $r \simeq 0.5$ for mesoscale currents [*Bidlot*, 2005].

Other indirect effects include a stronger wave dissipation in current fronts due to enhanced wave steepness [e.g., *Phillips*, 1984]. This effect can strongly modify wave modulation by currents, and it can be sensitive to the choice of parameterization [*Ardhuin et al.*, 2012]. All these effects have been verified with tidal currents where they are well known, for example in locations monitored by coastal radars [e.g., *Ardhuin et al.*, 2012].

Small-scale ocean dynamical patterns have been detected from remote sensing data [e.g., *Munk et al.*, 2000], but a quantitative evaluation of their magnitude and importance emerged only recently from the analysis of numerical model results [e.g., *Capet et al.*, 2016; *Klein and Lapeyre*, 2009; *Sasaki et al.*, 2014] and in

situ measurements [*Callies et al*., 2015], as reviewed by *McWilliams* [2016]. Our investigation was triggered by new satellite instruments that are being built or designed to measure the these small-scale currents via their sea surface height (SSH) signature [*Durand et al*., 2010], or a direct Doppler measurement [*Bourassa et al*., 2016; *SKIM Team*, 2016]. In this context, the measurement noise and possible errors are of particular interest, and some of these errors are related to waves [e.g., *Peral et al*., 2015; *Chapron et al*., 2005]. Our more general goal is to advance the understanding of the correlation between waves and currents, with a focus on open ocean scales ranging from 10 to 200 km, a subject that will certainly find other applications, probably for air-sea fluxes or extreme waves [e.g., *Romero et al*., 2017].

While recent studies have investigated the spatial variability of the mean square slope, which is dominated by waves around a meter in length [*Kudryavtsev et al*., 2012; *Rascle et al*., 2014], we focus on the significant wave height, which typically involves longer waves.

2. Wave Heights Over the Gulf Stream

Small-scale currents around the Gulf Stream have been the focus of much attention with the lateral mixing initiative [*Shcherbina et al*., 2015]. Although coastal currents at scales under 100 km can be monitored by high-frequency radars, there is no such data in the open ocean. We thus use numerical model output that is expected to be statistically consistent with the real ocean.

2.1. Current and Wave Model Setups

We use the ROMS model simulations presented by *Gula et al*. [2015], with a resolution of 1.5 km. These are nested in a lower-resolution simulation that spans the Atlantic basin. The simulation is forced by daily winds from a climatological year, diurnally modulated by surface fluxes, but without tides.

To evaluate possible biases due to model configuration, in particular oceanic forcing, we also use hourly currents in the Gulf Stream region from a global 1/48° resolution run of the Massachusetts Institute of Technology general circulation model (hereinafter MITgcm; see *Rocha et al*. [2016, Appendix D] for a brief description of this model settings). That configuration includes tidal forcing and 6 hourly atmospheric forcing from the 0.14° ECMWF atmospheric operational model analysis, starting in 2011. In the Gulf Stream region, horizontal grid spacing is 1.4 km.

Each surface current field is used to force a numerical wave model based on the WAVEWATCH III modeling framework [*WAVEWATCH III Development Group*, 2016], with 1/60° resolution in both longitude and latitude, and a spectral discretization into 24 directions and 32 frequencies, exponentially spaced from 0.0373 to 0.72 Hz. Simulations with 48 directions instead of 24 give 10–50% stronger gradients at scales 10–100 km, but these do not change our conclusions on the relative magnitude of the different processes. The wave model includes all four direct effects of current presented above, namely refraction, wave action conservation with a change in wave period, advection by the current, and the relative wind effect in the source term. The integration of the wave action equation (1) uses a splitting method [*WAVEWATCH III Development Group*, 2016]. We use a spectral advection time step of 25 s, used in particular for refraction, with a global integration time step of 200 s and a minimum source term time step of 5 s, and an advection time step of 50 s. We verified that further reducing all time steps had no significant impact on the model results.

In addition to currents, the wave model is forced by 3 hourly winds from the European Centre for Medium-Range Weather Forecasts (ECMWF) operational system, with 1/8th of degree resolution. This wind forcing is thus different from the wind used to force ROMS. Wave spectra at the offshore boundary come from the global wave modeling system and hindcast results described by *Rascle and Ardhuin* [2013]. Parameterizations for wave generation, dissipation, and other processes are consistent with that global hindcast, including later adjustments of the bottom friction [*Roland and Ardhuin*, 2014].

Wave conditions over the Gulf Stream are characterized by alternating young wind waves from nor'easter storms and old swells radiating from hurricanes [e.g., *Cardone et al*., 1996; *Herbers et al*., 2000; *Ardhuin et al*., 2003]. In order to sample both regimes, we have chosen to combine realistic wave forcing and boundary conditions for September 2014. Because of significant seasonal changes in the intensity of small-scale currents, we investigate the impact of ROMS current for September and June on our September waves.

2.2. Effects of Currents on Waves

Figure 1 shows a typical example of modeled significant wave heights in the case of swells from a remote storm, in this case from the 2014 Hurricane Edouard. While the storm remained east of 57°W, in the middle of the Atlantic, swell propagated west to the North Carolina Outer Banks. Except for the bottom topography effects (refraction and bottom friction) that are confined to the continental shelf [e.g., *Ardhuin et al.*, 2003], wave height patterns in Figure 1a are dominated by the effects of currents. In particular, the Gulf Stream and the two current rings shown in Figure 1b have a clear correspondence with the current influence on wave heights shown by Figure 1c, as studied previously by *Holthuijsen and Tolman* [1991]. The warm-core ring, to the north, is spinning clockwise while the cold-core ring, to the south, is anticlockwise. The particularly strong reduction in wave height marked by the arrow in Figure 1e is due to refraction over the ring, and is slightly reinforced by the smallest scales of the current field (Figure 1f).

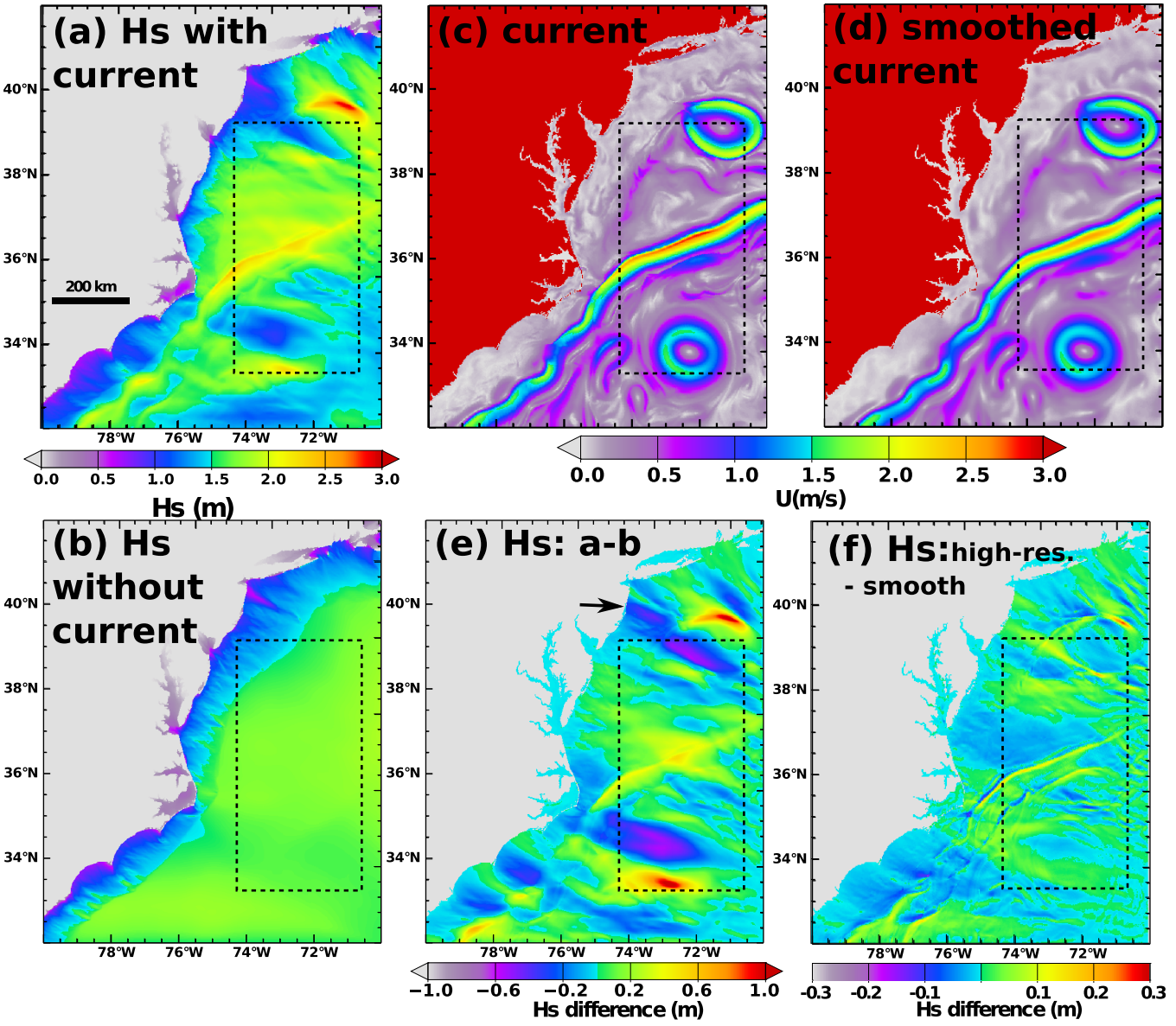

Figure 1. Impact of current on swells across the Gulf Stream on 18 September 2014, 6:00 UTC. Maps of (a) modeled wave height, (b) wave height from model without current, (c) high-resolution current from ROMS, (d) same current field smoothed. (e, f) Wave height difference for (e) case with high-resolution current minus case without current and (f) cases with high-resolution current minus case with smoothed currents. The dashed box is the region used for the spectral analysis shown in Figure 2.

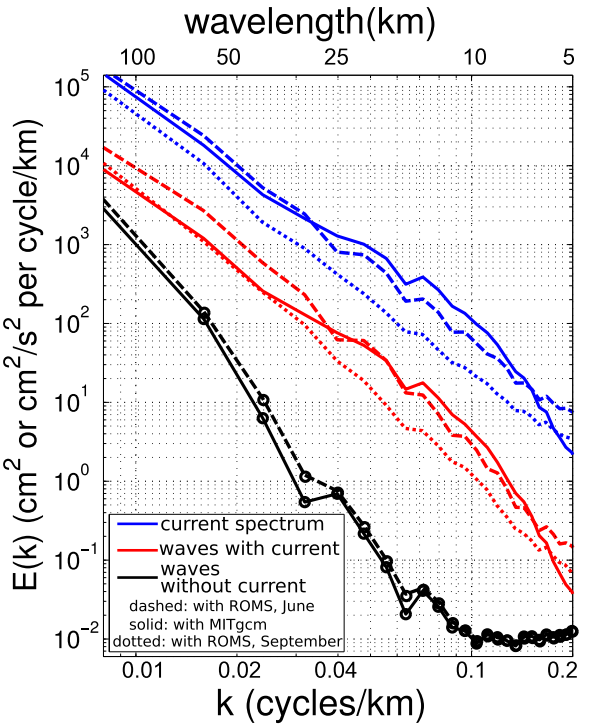

Figure 2. Omnidirectional time-averaged spectra of current and H_s for the Gulf Stream, when current effects of waves are included (in red) or without current effects (black). Dashed or dotted lines and solid lines correspond to currents from ROMS or MITgcm, respectively. Two-dimensional spectra computed over the rectangular box ranging from 74°W to 71°W, and 33.7 to 38.7° were converted to a single dimension by gathering the variance of spectral components of all directions that have the same wavelength.

The map of wave height differences in Figure 1e includes both large and small-scale features. Smoothing the current to remove details with wavelengths of 10 km or shorter (see Figure 1d) has a visible impact on the wave heights with variations up to 10% (Figure 1f). These include far-field effects along the shoreline. From the North Carolina Outer Banks to Cape Cod, ocean currents and their details at scales of the order of 10 km significantly affect nearshore waves. This has implications for extreme events and storm surges [e.g., *Hall and Sobel*, 2013].

In order to quantify the effects of currents, we analyze the spectra of spatial variations of currents and wave heights. Power spectral densities were computed from the two-dimensional Fourier transforms over a set of 3×3 tiles covering dashed box in Figure 1, after a Hann window has been applied along each dimension for each tile. The variance lost due to this windowing is corrected by rescaling the resulting spectra, which are then averaged in time to reduce their statistical uncertainty. The two-dimensional average spectra were then binned into one-dimensional (1-D) spectra by summing the variance in wave number bands with a constant resolution, corresponding to a sum over all possible directions. These 1-D spectra represent the distribution of variance across spatial scales. The shortest resolvable wavelength is twice the grid spacing, $L = 3$ km or $k = 0.33$ cycles per kilometer (cpk). The results are shown in Figure 2 and are only significant for $k < 0.1$ cpk due to the numerical dissipation of small scales in the ocean circulation models, which is the likely cause of the change in spectral slope around $k \simeq 0.15$ cpk. The two circulation model results are similar (MITgcm: solid, ROMS: dashed for June currents, dotted for September currents) and have the same impact on wave heights. The nearly constant slope of the current spectrum between wavelengths of 100 and 10 km suggests that both ROMS and MITgcm resolve correctly those scales, while the change in slope between 5 and 10 km wavelength is probably associated with the numerical dissipation [e.g., *Capet et al*., 2016].

A striking property revealed by Figure 2 is that in our model that takes into account currents (in red), the spatial variability at 100 km scales is 4 times higher than in the model without currents (in black): in other words, currents account for more than 75% of the spatial variability of wave heights at scales of 100 km in our model. This proportion increases dramatically for shorter scales and exceeds 99% at 25 km. Also, the spectrum of H_s closely follows the shape of the current spectrum. Simulations using high-pass or low-pass velocity fields (not shown) confirm that the shape of the H_s spectrum adjusts to the current spectrum, and the two are roughly proportional for wavelengths between 10 and 100 km.

One would think that this variability of H_s could be easily validated with satellite altimeter data, but this is generally not the case for scales shorter than 100 km [*Sandwell and Smith*, 2005]. Figure 3 shows examples of observed variability in H_s that is associated to the Gulf Stream, and spectra of H_s over our region of interest. Figure 3b shows a very large increase in wave height as waves from a nor'easter storm encounter the Gulf Stream. For reference, the wave model hindcast of *Rascle and Ardhuin* [2013] has values of H_s that do not exceed 3.5 m in the current for that day (without current effects). In that hindcast, which has a resolution of 1/6° of the Gulf Stream, including forcing by altimeter-derived geostrophic currents [*Rio et al*., 2014]

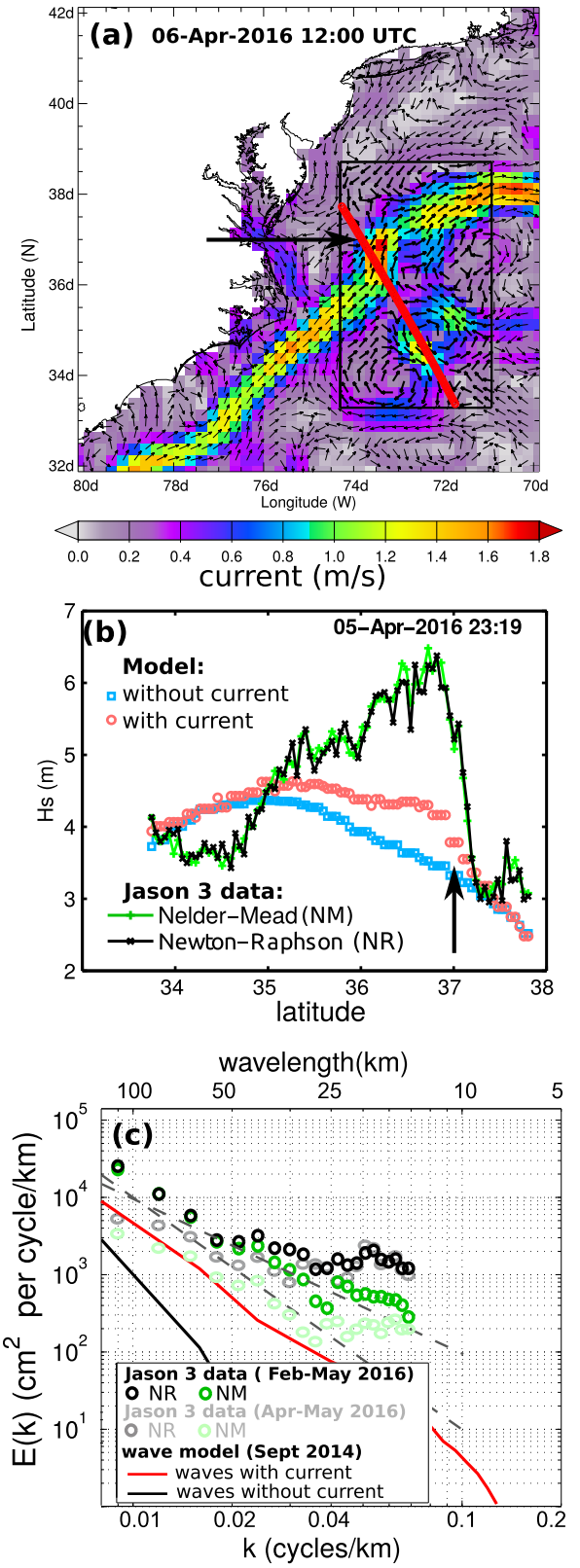

Figure 3. Example of (a) surface geostrophic current produced for the Globcurrent project and provided by AVISO [*Rio et al.*, 2014], overlaid with the Jason-3 track of 5 April (red circles) and (b) variation of H_s along a Jason-3 altimeter track, as given by the standard Newton-Raphson method (NR) or an alternative Nelder-Mead method (NL). (c) Spectra H_s for Jason 3 cycles 1–11 (February–May) or 8–11 (April–May). The arrows in Figures 3a and 3b mark the location where the satellite track crosses the northern edge of the Gulf Stream.

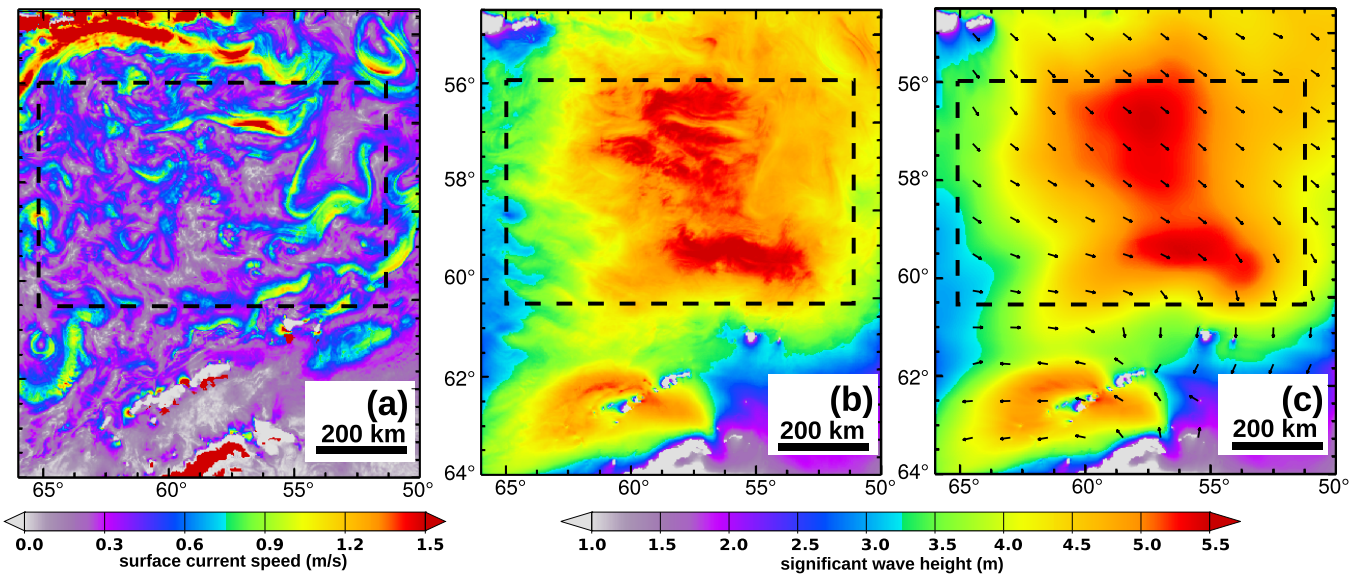

Figure 4. Maps for 16 September at 18:00 UTC for (a) surface current magnitude modeled by MITgcm, (b) the modeled significant wave height when the current forcing is included in WAVEWATCH III, (c) wind direction from ECMWF (arrows) and modeled significant wave height without effects of currents. The dashed box is the region used for spectral analysis.

introduces a clear gradient of H_s around 37°N. Still, that modeled gradient is only half of the measured gradient, probably because of the limited resolution of the current field, and also because of the geostrophic approximation [e.g., *Penven et al*., 2014, Figure 9]. One of the modeled patterns discussed in Appendix B (Figure 10e), also for a nor'easter event, is closer to this observed situation.

With the higher-resolution simulation presented here, we can only attempt a statistical validation, for example with the spectra of H_s derived from altimeter. These spectra are very sensitive to the retracking method for wavelengths shorter than 100 km. A comparison of the standard Newton-Raphson processing with a Nelder-Mead numerical retracker is shown in Figure 3c (experimental data provided by CNES). It demonstrates that the standard processing produces a background spectral noise of about 2000 cm^2 per cycle/km, so that the spectrum of H_s is dominated by noise for scales shorter than 100 km when the wave height is low (e.g., April–May 2016, which is similar to September 2014). For larger wave heights, the spectrum decreases like k^{-3} down to wavelengths of 40 km. These observed spectral shapes are consistent with our model results that include currents.

3. Wave Heights in Drake Passage

From the analysis of the Gulf Stream region only, it is unclear how general these conclusions are, and what to expect for different regimes of ocean circulation or waves. Because the MITgcm simulation is global, we can investigate the relationship between currents and wave parameters in other regions. We have chosen to focus on Drake Passage, between South America and Antarctica, because the MITgcm simulation has been analyzed in detail for that region by *Rocha et al*. [2016]. These authors found the currents to be statistically consistent with in situ ADCP data, and we thus expect that current patterns are generally realistic.

Drake Passage is a good example of an open ocean region with a strong current, energetic mesoscale and submesoscale variability, and large swell from the Pacific. For our analysis of wave-current interactions, we consider a rectangular box from 56°S to 60.5°S and 51°W to 65°W, as illustrated in Figure 4. This box is located south of the strong flow associated with the Sub-Antarctic Front (SAF), which hugs the coastline and carries a significant transport through Drake Passage. In order to limit the direct contribution of large-scale currents, we chose a box away from the SAF for our spectral analysis, but it contains eddies that radiate from the SAF. A weaker structure, the Polar Front (PF), is located roughly in the center of Drake Passage, between 58°S and 60°S and does not stand out so much in surface velocities, because it meanders substantially [e.g., *Dong et al*., 2006].

3.1. Model Setup

In Drake Passage as over the Gulf Stream, our wave model uses the WAVEWATCH III framework [*WAVEWATCH III Development Group*, 2016], here configured to have the same spatial resolution as the MITgcm grid, meaning a local resolution of 1.4 km, with other properties unchanged from the Gulf Stream run, except for a spectral advection (i.e., refraction) time step reduced to 12.5 s instead of 25 s. This is because we had one test with 48 directions instead of 24, and we kept the time step the same for consistency. The open boundaries are forced by wave spectra from a 0.5° resolution global run that does not include currents, and that is forced, besides the MITgcm currents, by ECMWF winds, sea ice concentration from NCEP, and iceberg distributions from Ifremer [*Ardhuin et al.*, 2011]. We performed tests with higher-resolution winds (5 km, hourly), which showed that small-scale wind variability contributes little to the wave height variability (see Appendix A).

The simulation spans 10–30 October 2011. We allow the wavefield to spin-up for 3 days and analyze the period from 13 to 18 September, which is representative of the entire run.

3.2. Spatial Patterns of Wave Heights

Over large-scale currents like the Gulf Stream, the deflection of wave rays by refraction easily produces large gradients in wave heights at a scale that is related to the "focal distance" and the coherence scale of the current [*White*, 1999; *Gallet and Young*, 2014]. It is more surprising to find large gradients with smaller-scale currents. Figure 4b shows that the modeled wave heights have patterns on the same scale as the surface current shown in Figure 4a. This variability in the presence of currents contrasts with the smooth H_s field in the case without current, shown in Figure 4c. Without current, wave heights are generally smoother than the wind field [*Abdalla and Cavaleri*, 2002], except in locations that experience blocking by land, islands, or icebergs [*Tolman*, 2003; *Ardhuin et al.*, 2011].

The explanation of this variability in wave heights can be obtained by the spectral analysis of the current and H_s maps, and the deactivation of various processes in the model. In order to avoid land and boundary effects, this analysis is restricted to the dashed box in Figure 4.

The shape of the mean meridional H_s spectrum exhibits a transition at a wavelength of 80 km from a decrease like $k^{-0.5}$ for large scales to k^{-3} for smaller scales (red curve in Figure 5a). With its narrow footprint, the AltiKa altimeter has provided wave heights with unprecedented accuracy since its launch in 2013 [*Sepulveda et al.*, 2015]. We thus use AltiKa data for the same region but over the full year 2015 (202 tracks) and find a similar transition but at a larger wavelength of 120 km (Figure 5a). At wavelengths shorter than 70 km, the raw 1 Hz data that we use here are contaminated by noise, which explains the nearly flat

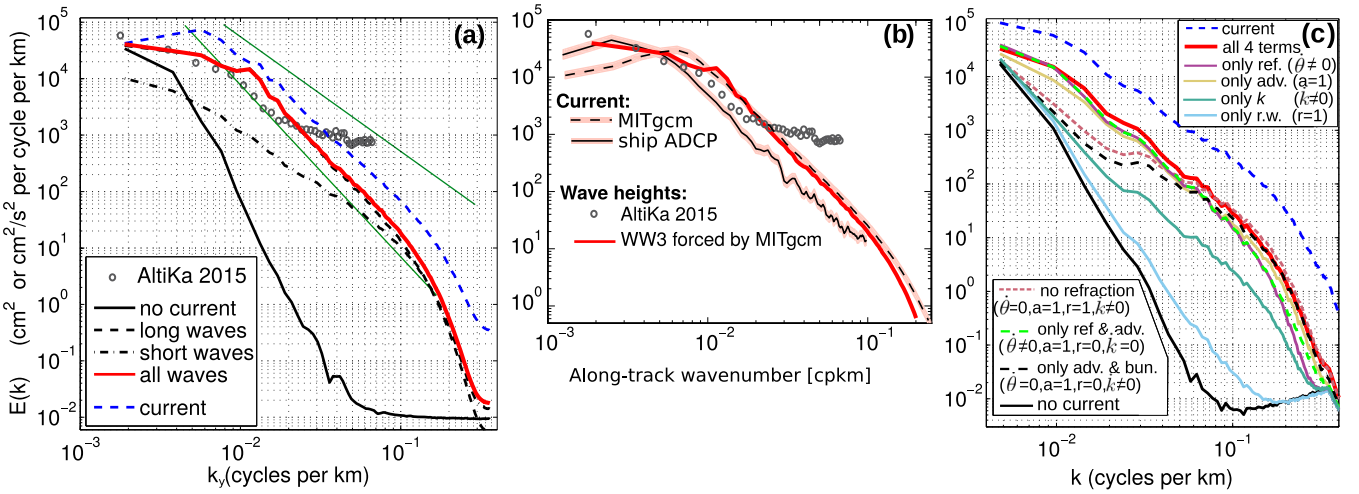

Figure 5. Spectra of current and wave heights for Drake Passage. (a) Spectra of modeled zonal current and H_s along the north-south direction, with contributions of waves of periods shorter or longer than 6 s, along-track measured spectrum from AltiKa is shown for comparison, and power laws k^{-2} and k^{-3} are shown in green. (b) Wave height spectra from panel a overlaid on current spectra from *Rocha et al.* [2016, Figure 6], showing a similar—but smaller—shift of the modeled spectra compared to the measurements. (c) Omnidirectional spectrum of H_s and contributions of the current through the four different terms of the wave action equation (1) can be revealed by progressively switching off the different terms: refraction $\dot{\theta}$, change in wave number $\dot{k}$, relative wind r, and advection by u_E and v_E in $\dot{\lambda}$ and $\dot{\phi}$.

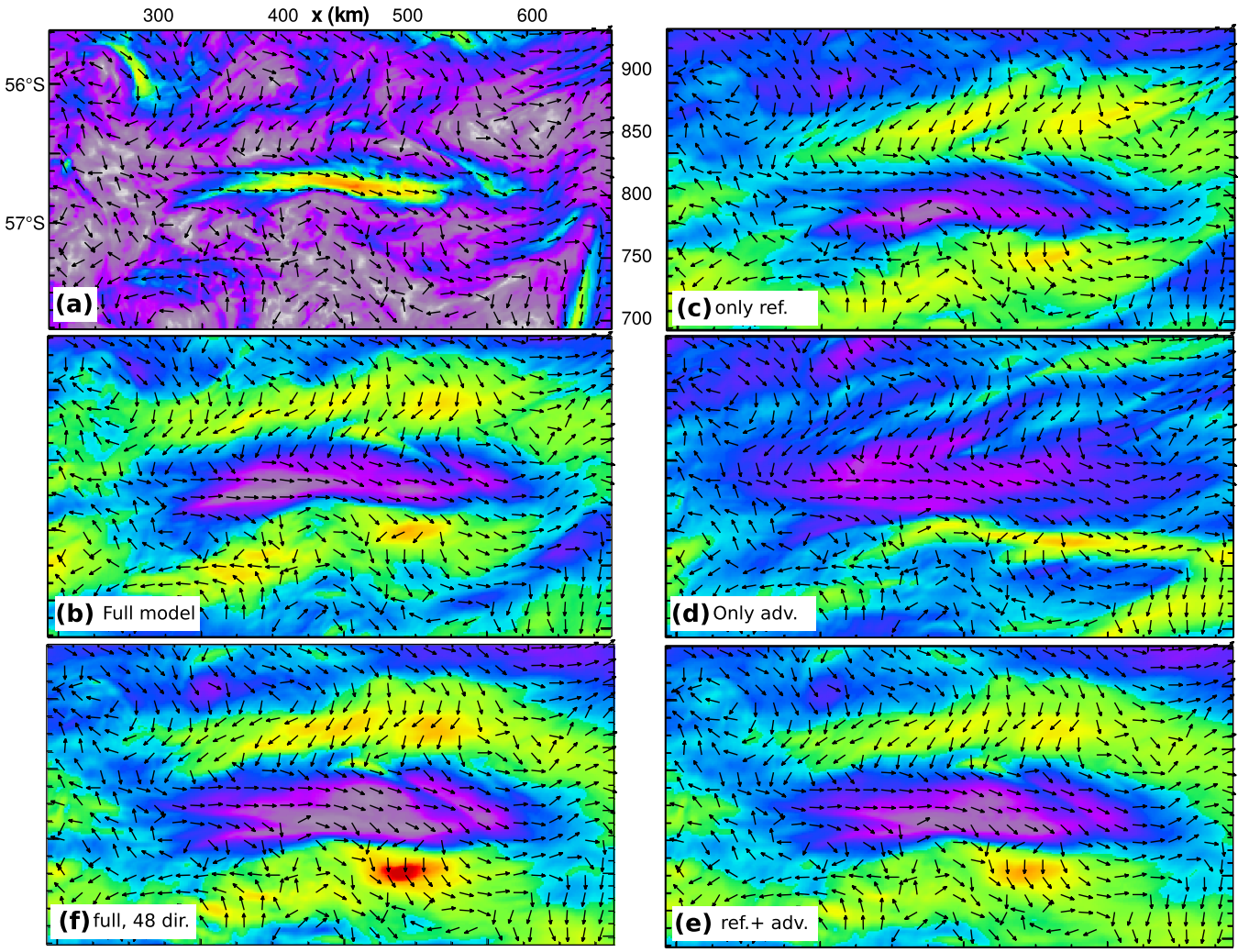

Figure 6. Example of current patterns and adjustment in wave height for model snapshots at 23:00 on 14 September 2011. Figure 6a shows the current magnitude, and arrows indicate the current direction for one out of 10 pixels in each direction. The same arrows are overlaid on other panels. Wave height response in Figures 6b–6e correspond to Figure 6b the full model, the (c) model with refraction only, (d) only advection by currents, and (e) refraction and advection. The effect of directional resolution is also evaluated in Figure 6f with a simulation in which only the number of direction has changed, from 24 to 48 directions.

spectrum for $k > 0.02$ cpk [*Dibarboure et al*., 2014]. The difference between spectra of model and observed H_s at scales around 100 km is similar to the difference reported by *Rocha et al*. [2016, Figure 6, partly reproduced in Figure 5b] between the 1999–2012 ADCP velocity spectra and the MITgcm simulation. This suggests that modeled wave height would better fit the AltiKa data if the MITgcm were corrected for a distorted kinetic energy spectrum around 100 km wavelength.

Because the wavefield contains a wide range of scales, each with its own spatial pattern, we can distinguish between the different wave components by computing the spectrum of an equivalent wave height estimated from the short waves H_{ss}, using dashed and dash-dotted curves for f_c=0.17 Hz in Figure 5a. The long waves dominate the variability of H_s for scales larger than $L_c = 6$ km, whereas the short waves dominate the smaller scales. This variability is consistent with the idea of a longer relaxation scale for the longer waves, as used for example by *Kudryavtsev et al*. [2005] for remote sensing applications. Shifting f_c to lower frequencies increases the scale L_c.

The omnidirectional spectra in Figure 5b also follow a k^{-3} power law from 100 to 10 km wavelength, comparable to the $k^{-2.7}$ of the velocity spectrum. Both spectra exhibit a sharp roll-off at wavelengths less than 10 km due to the effective numerical resolution of the MITgcm currents, with the smallest scales artificially damped by the numerical scheme of the model. The spectrum of H_s is roughly 0.2 s^{-2} times the current

spectrum. Rerunning the model with and without the different current effects, we diagnose the different physical effects, as shown in Figure 5b. This decomposition into the different terms is not sensitive to the pattern orientation, as zonal gradients (not shown) or omnidirectional spectra (Figure 5b) give the same ordering of the various processes.

Because the combination of the different processes is not linear, it is difficult to attribute a well-defined part of the wave height gradients to any of the explicit terms in equations (2)–(5), given that there is also an indirect effect via the dissipation rate which is part of the wave action source term S in equation (1). Still, it appears clearly that at scales larger than 20 km one of the dominant effects is from wave turning due to refraction: including only refraction (setting the other three terms to zero) gives a spectrum of H_s that is within a factor 2 of the full model for these scales, and removing only refraction reduces the variance by a factor 3 or more. However, the refraction effect is partially canceled by the advection term, which taken alone would explain nearly half of the variance at all scales. Overall, refraction and advection dominate together for scales larger than 30 km. In contrast, at scales shorter than 20 km, the dominant effect on the variance of H_s is advection, which is partly canceled by refraction but enhanced by the velocity bunching (concertina effect) and the relative wind effect.

To illustrate the partial cancellation of refraction and advection, we have included one example of wave height patterns in the middle of our region of interest (Figure 6). Please note that the arrows in all panels correspond to the current direction. This snapshot includes a strong westerly jet (in yellow and orange at the center of Figure 6a), which gives a lower wave height in the jet (in gray and purple at the center of Figure 6b) and higher wave heights on both north and south sides of the jet (in green and yellow). This pattern of wave height is mostly due to refraction as shown in Figure 6c: the waves are mostly from the west at this time and are turning toward both sides of the jet. The effect of advection by currents is more complex, because the divergence of the energy flux $\partial((C_g+U)E)/\partial x$ depends on the gradients of the energy, which are also determined by refraction. As a result, the difference in wave height due to refraction and advection is not the simple sum of the differences due to each process. When combined (Figure 6e), they explain most of the effects of currents in the full model (Figure 6b).

These results are qualitatively robust to changes in model settings. Yet, given the importance of refraction, reducing the directional resolution to 7.5° (48 directions) instead of 15° (24 directions) produces an enhancement of wave height gradients, as shown in Figure 6f. The spectrum in Figure 7a reveals that this enhancement only occurs for scales larger than 10 km. The finer directional resolution is not necessarily more realistic. Indeed, in coastal simulations with currents *Ardhuin et al*. [2012] have found a general underestimation of the directional spread, possibly due to wave scattering by currents. If this is also the case here, an underestimation of the directional spread would produce an overestimation of the gradients of H_s induced by refraction.

Refraction is responsible for the relatively strong gradients of energy for long period waves compared to shorter periods (Figure 7b). It is interesting to see the spectra of the various moments of the wave spectrum. These are defined from the full wave spectrum as

$$E(f)=\int_0^{2\pi}\sigma N(k,\theta)\frac{\partial k}{\partial f},\mathrm{d}\theta, \tag{7}$$

$$m_n=\int_{f_{\min}}^{f_{\max}}E(f)f^n\mathrm{d}f, \tag{8}$$

where $f=\sigma/2\pi$ is the wave relative frequency (frequency in the frame of reference moving with the surface current). Figure 7b shows the spectra of m_n with n ranging from 0 to 4. We recall that the significant wave height is defined by $H_s=4\sqrt{m_0}$ and that the mean square slope is proportional to m_4. These five moments have a similar root mean square relative variation at scales shorter than 100 km, between 4 and 5%, yet, the higher moments, such as m_4 have a stronger variation at small scales.

The general similarity of spectra of current and wave heights was already found around the Gulf Stream. We investigated the variability of the energy level around 10 km wavelength by integrating a whitened spectrum (multiplied by k^3 to compensate for the average power law) over wavelengths 8–12 km. This

yields representative energy levels E_H and E_U for wave heights and currents, respectively, every 1 h. The temporal variability of these two energy levels can be related by the following expression (Figure 8):

$$E_H \simeq 70 \frac{\langle H_s \rangle^2}{g^2 \langle T_{m0,-1} \rangle^2} E_U, \tag{9}$$

where the angle brackets refer to a spatial average, and the mean period $T_{m0,-1}$ is defined from the wave moments as

$$T_{m0,-1} = m_{-1}/m_0. \tag{10}$$

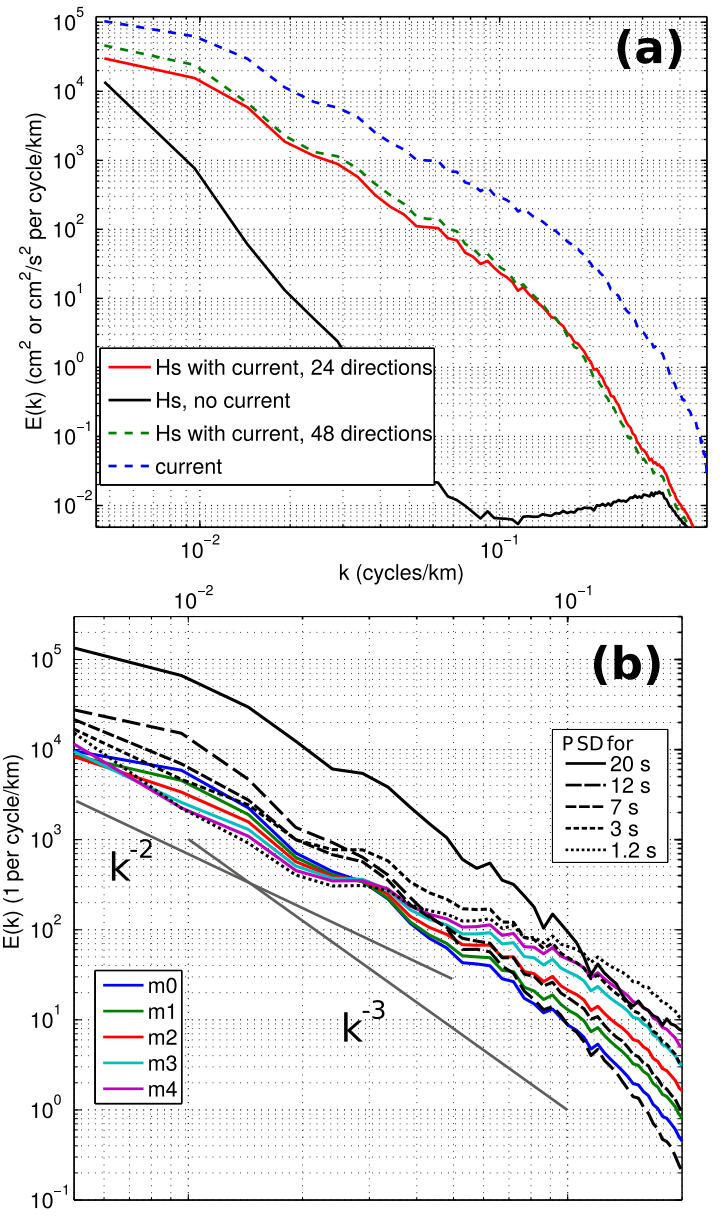

Figure 7. (a) Same as Figure 5, showing the difference in spectra of H_s when running the model with 24 or 48 directions. (b) Spectra of wave power spectral density (PSD) $E(f)$ for periods 20–1.2 s (black lines with various line types), and spectral moments m_0 to m_4 (color) given by equation (8) with f_{min} =0.037 Hz and f_{max} =0.72 Hz. In Figure 7b all spectra were computed after dividing the field at each time step by its mean value, and all were obtained with 24 directions.

The empirical relationship given by equation (11) expresses the general increase in wave variability with the average wave height, and a stronger impact of currents for shorter periods. In the case of the Gulf Stream, the wave height patterns change with the wave conditions from the shorter period nor'easter storms to longer swell periods. This relationship is given here as a rule of thumb for obtaining an order of magnitude of the wave height variability. There are certainly other factors in addition to the current spectrum and the mean period that contribute to the variability of H_s. In particular, the high outliers with $E_H/E_U > 0.2$ s^2 appear to correspond to northeasterly winds around 12 m s^{-1} blowing against the Gulf Stream on 27 September. This case is discussed in Appendix B. Such outliers are not present in wave model results forced by the same winds but using MITgcm currents. Our hypothesis is that the local intensity and alongstream coherence of the ROMS simulation are the main reason for this difference. *White and Fornberg* [1998] have shown that current coherence can be an important factor in the patterns of wave heights due to refraction.

The empirical relationship formulated in equation (11) is also consistent with advection and velocity bunching effects. Indeed, for monochromatic waves of

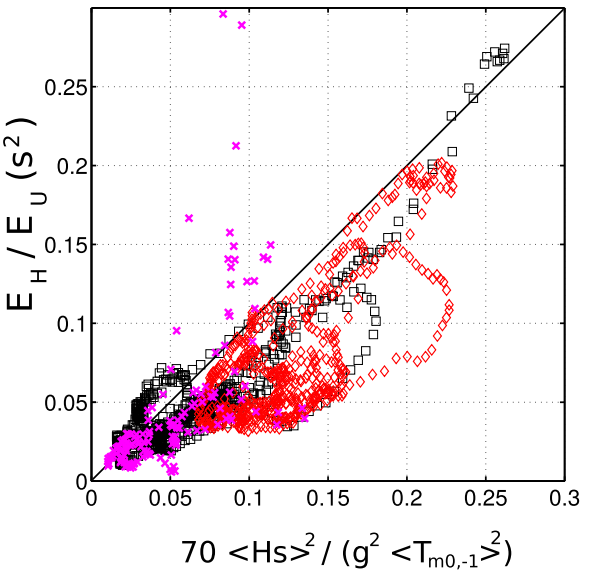

Figure 8. Ratio of wave height and current spectra at scales around 10 km, as a function of the spatially averaged wave height and energy period. Red diamonds: Drake Passage (15 September to 8 October 2011, magenta crosses: Gulf Stream with ROMS (September 2014), black squares: Gulf Stream with MITgcm (October 2011).

phase speed $C=gT/2\pi$, neglecting dissipation effects, the conservation of wave action over a stationary current with $\boldsymbol{u}_E$ that varies in the direction of wave propagation gives a change in wave height $\Delta_H=4\pi u_E H_s/gT$. This theoretical relationship corresponds to equation (11) with, for example, $\langle H_s\rangle=4$ m and $\langle T_{m0,-1}\rangle=10$ s. However, because the current gradient is not generally aligned with the wave propagation direction, this effect only explains part of the empirical relationship.

Equation (11) gives an order of magnitude of wave height fluctuations, but it says nothing about the pattern of wave heights and its deterministic relation to the pattern of currents. A more detailed inspection (not shown) reveals an average correlation $r^2 \simeq 0.5$ at scales under 20 km between wave heights and the current projected in the wind direction, such that wave heights decrease when the current increases in the wind direction. Hence, beyond a prediction of the spectral shape of H_s, it may be feasible to predict most of the small-scale wave patterns without running a full spectral wave model.

Overall, patterns of H_s in our simulations are dominated by the effect of mesoscale currents, with wavelengths larger than 50 km, confirming the analyses of *Mapp et al*. [1985], *Gutshabash and Lavrenov* [1986], and others. At shorter scales, the relative wind and advection effects become more important. Previous discussions of H_s gradients have emphasized the importance of wind variability [*Abdalla and Cavaleri*, 2002] or nonlinear wave evolution [*Badulin*, 2014; *Kudryavtsev et al*., 2015]. Our results suggest that current effects cannot be ignored at scales shorter than 200 km. Joint observations of wind, waves, and currents and fully coupled models are needed to evaluate the magnitude of each of these three effects.

3.3. Extreme Values of H_s

Without performing a detailed analysis, which is beyond the scope of the present paper, we note that fluctuations at small scales produce maxima values of H_s that are larger when currents are taken into account. In simulations with a current smoothed to remove scales shorter than 10 km, differences in the distribution of H_s occur above 6.4 m, corresponding to the 96th percentile. The 99th percentile of the H_s distribution increases by 2% from 6.67 to 6.79 m when currents are included, and it is 6.76 m for smooth currents. The dominant effect in the maximum values of H_s is refraction. When the full resolution current is used but refraction is deactivated, the 99th percentile is actually lower, at 6.59 m. It is the creation of "caustic-like" features due to refraction, as discussed by *White and Fornberg* [1998] that creates the maximum values of H_s. Due to refraction, the local maxima of H_s are generally associated with increased directional spreading. The impact of these correlations on the extreme values of individual waves is beyond the scope of the present paper, but varying directional properties should be considered together with the distribution of significant wave height [e.g., *Waseda et al*., 2011; *Mori*, 2012]. From the differences found between ROMS and MITgcm in the Gulf Stream region (see Appendix B), we expect that the current intensity and structure can also have a strong impact on the maximum values of H_s.

4. Implications for Remote Sensing

Several techniques have been proposed to estimate the variability of currents at scales smaller than 100 km. Here we will consider two of these, the measurement of sea surface height, and the

measurement of geophysical anomalies in the Doppler centroid [*Chapron et al*., 2005]. Both techniques involve a sea state bias, which may require some knowledge on the wavefield evolution at small scales.

4.1. Currents From Altimetry at Scales Under 100 km

Estimates of the ocean circulation from altimetry have been very successful for large scales, but the wavelengths under 200 km are affected by a variety of noise sources. Some of these errors are correlated with H_s, either due to the processing of the waveforms or due to the correction of the sea state bias using the noisy estimates of H_s. A correction proposed by *Sandwell and Smith* [2005] assumed that H_s "should be very smooth over length scales less than a few hundred kilometers." This assumption is contradicted by our finding that the wave heights are not smooth at scales of 50–100 km due to currents. With a correlation of H_s and currents, and thus sea surface height, the method proposed by *Sandwell and Smith* [2005] might remove a significant part of the sea surface height signal.

With future satellite missions such as Surface Water Ocean Topography (SWOT) satellite mission [*Durand et al*., 2010], the small-scale gradients of H_s may be an important source of error via the systematic range error known as sea state bias (SSB). That error can be reduced with accurate estimates of wave parameters both along and across the satellite track. Airborne measurements [*Vandemark et al*., 2005] give a sea state bias (SSB) in Ka-band that is of the order of 3% of the significant wave height H_s [*Valladeau et al*., 2015]. Without any information on the cross-track variations in H_s, and assuming that the SSB is fully determined by H_s alone, the spectrum of range error at 50 km away from the nadir would be 0.03^2 times the wave height spectrum shown in Figure 2. Over the Gulf Stream, this can be 1 cm^2/(cycle/km) for $H_s = 2$ m at 50 km wavelength. This value should be compared to the baseline total error level of 5 cm^2/(cycle/km). The planned onboard estimation of wave-related variables, necessary to evaluate SSH noise [*Peral et al*., 2015], can thus be adjusted to mitigate errors in SSB corrections.

We expect that the empirical relationships used for altimeter SSB at large scales [e.g., *Tran et al*., 2010] do not apply at small scales because the sea state variability at small scales will be dominated by current instead of wind patterns. Also, the variations of SSB should be controlled by wave-related parameters other than just H_s [*Melville et al*., 2004]. As shown in Figure 7b, the wave parameters that are more strongly weighted by high frequencies have stronger relative gradients at small scales, because higher-frequency waves vary more strongly at small scales (Figure 5a). This is the case of the surface Stokes drift U_{ss}, which is almost proportional to m_3 [*Ardhuin et al*., 2009], or the mean square slope (mss), proportional to m_4. In Drake Passage and at scales around 10 km, the spectrum of H_s decays like k^{-3} compared to k^{-2} for U_{ss} and $k^{-1.5}$ for the mss. Hence, the investigation of SSB variations at small scale should be restarted from basic principles. This can be done using the kind of simulations performed here and following the theory put forward by *Longuet-Higgins* [1963], as applied by *Srokosz* [1986].

4.2. Direct Doppler Measurements of Currents

Chapron et al. [2005] have used the Doppler centroid of radar backscatter from the sea surface to measure surface currents. In principle, this technique can perform better than altimetry for small scales, because there is no need to take a gradient of the measured quantity, and it provides measurements where the geostrophic relation between sea level and currents does not hold, at the Equator. However, the Doppler centroid contains a wave-induced bias that is G times the surface Stokes drift U_{ss}. The gain factor G changes with the radar band used, and it decreases with increasing incidence angle of the measurement. The Envisat SAR data analyzed by *Chapron et al*. [2005] use C-band at 23° incidence and have $G \simeq 20$. Values for future satellite missions proposing to use Ka-band range from $G \simeq 10$ at 58° for the Wind and Current Mission [*Bourassa et al*., 2016] to $G \simeq 45$ at 12° for the Surface Kinematics Multiscale monitoring mission [*SKIM Team*, 2016].

The retrieval of surface currents thus requires an estimate of U_{ss}, especially at small incidence angles. Based on the Gulf Stream simulations, we find that the spectral level E_{Uss} of U_{ss} is strongly correlated to the spectral level E_U of the current ($r = 0.94$ for September). The proportionality coefficient between the two spectra increases toward smaller wavelength as the spectrum of U_{ss} decreases like k^{-2} while the current spectrum is slightly steeper. Around 10 km we find,

$$E_{Uss} \simeq 0.03\mathrm{m}^{-1}\mathrm{s} \quad \langle U_{ss} \rangle E_U. \tag{11}$$

We now consider the case of Ka-band and 12° incidence, corresponding to SKIM, and using the mean spectrum of U_{ss} over the Gulf Stream in September. A lack of knowledge of U_{ss} variability at wavelengths less than a cutoff L_c gives a residual root mean square error of $G\Delta U_{ss}$=30 cm/s in the direction of the Stokes drift vector, if L_c = 100 km and 18 cm/s if L_c = 40 km. These errors are smaller than the relative root mean square fluctuations of the order of 60 cm/s after a correction based only on wind speed alone, as used by *Collard et al.* [2008] for a single SAR pass. This is why *Rouault et al.* [2010] had to average many SAR scenes treated with that technique in order to obtain reliable current estimates. Hence, the use of a lower incidence angle, for example 12°, can yield accurate currents, provided that the Stokes drift vector is estimated accurately every 50 km (corresponding to a wavelength of 100 km). This Stokes drift can be obtained from a directional wave spectrum measurement.

5. Conclusions

Realistic numerical wave model simulations in the Gulf Stream and Drake Passage regions have revealed that the variability of significant wave heights in the open ocean can be dominated by the effects of ocean currents at scales of 10–100 km. This modeled variability is consistent with the variability of altimeter-derived wave heights which is accessible for wavelengths larger than 50 km in large sea states. In the cases investigated here, refraction is the dominant effect for scales larger than 50 km, overtaken by advection effects for shorter scales. In general, flow intensity and structure have an impact on the wave height gradients. These findings provide a novel view of oceanic sea states at small scales that is relevant for the investigation of coastal hazards, extreme wave heights, and remote sensing, and may be relevant for the coupled evolution of surface waves and mixed-layer processes [e.g., *Rascle and Ardhuin*, 2009; *Suzuki et al.*, 2016].

A clear limitation of the present results is the absence, in our model, of some processes that are known to be important for wave evolution. One of them is the correlation between currents, temperature gradients, and wind speed [e.g., *Chelton et al.*, 2004], which may have an impact on wave growth. As a result, the relative wind effect that we use is only an order of magnitude estimate that neglects the adjustment of the wind to the local currents and temperature gradients. Another possible process is the enhancement of wave-induced mixing and drift [e.g., *Rascle and Ardhuin*, 2009] in the upper ocean, which can influence the evolution of ocean submesoscale circulation features [*Suzuki et al.*, 2016].

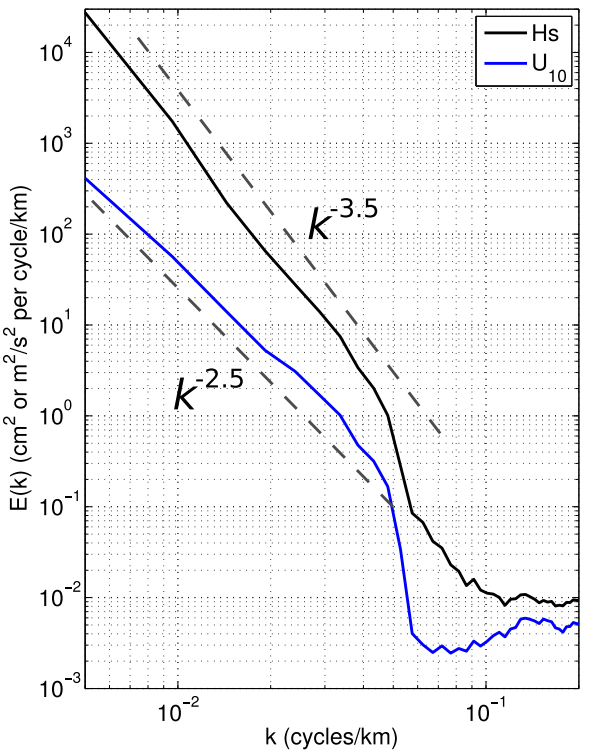

Figure 9. Spectra of wind speed U_{10} and wave height H_s in Drake Passage, without current, for an IFS simulation using the cubic octahedral grid with a 5 km resolution.

There is thus a clear need for fully coupled ocean-wave-atmosphere modeling, guided by the investigation of high-resolution measurements. Data from satellite altimeters that do not use Doppler are probably insufficient for the investigation of scales under 50 km, even with the retracking algorithms proposed so far. Delay-Doppler altimeters such as Cryosat and Sentinel-3 can provide data on the joint along-track variations of H_s, mss, and sea surface height at scales under 100 km, which may shed some light on the real importance of the various wave-current-atmosphere interactions processes. The recent analysis of satellite optical imagery by *Kudryavtsev et al.* [2017] has shown that current-induced variations in wave heights at these scales can be observed. Exploiting

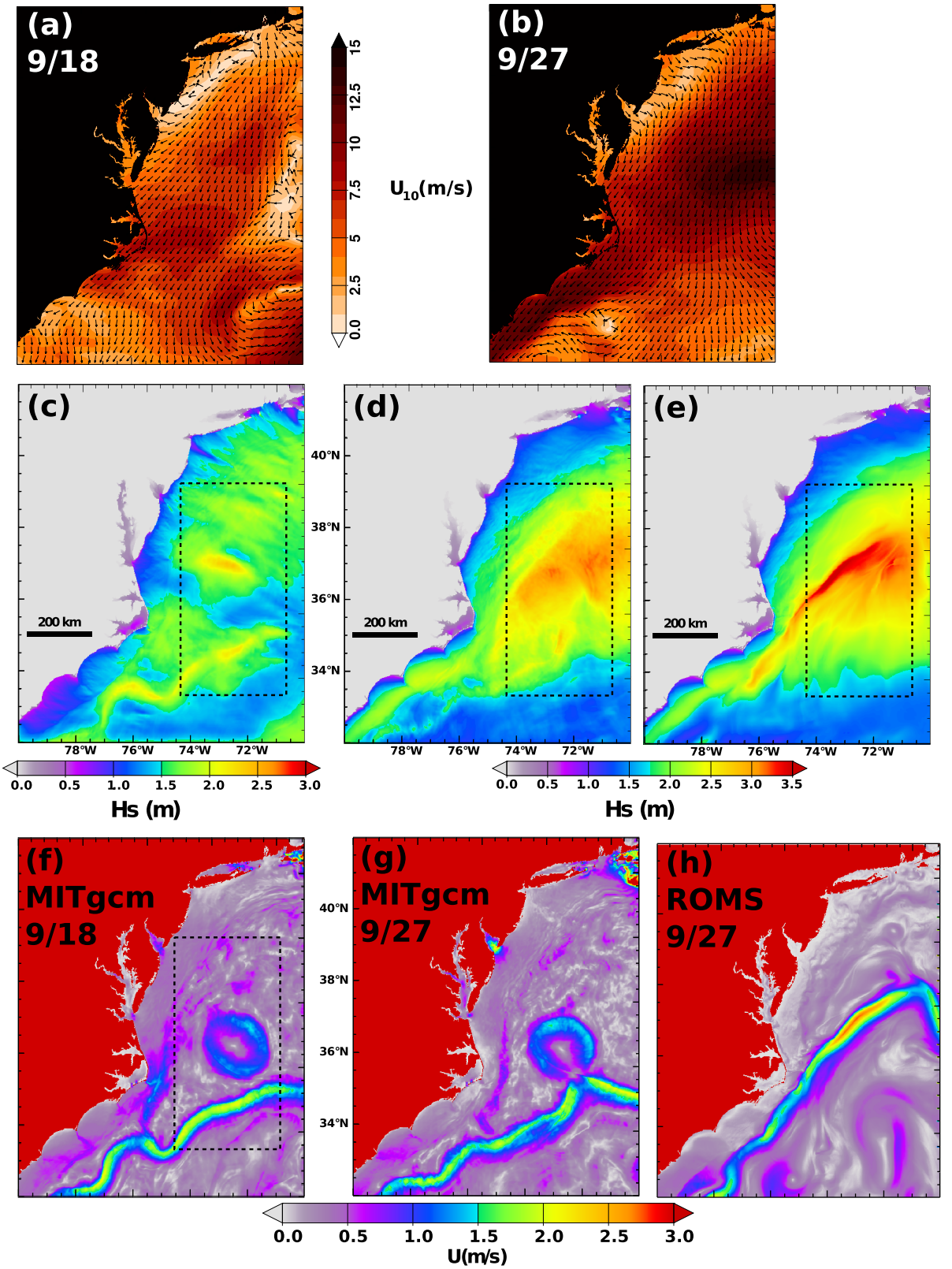

Figure 10. Impact of currents on waves for swell (on 18 September) and local wind-generated waves (on 27 September). The ECMWF analyzed wind fields on 18 September at 6:00 UTC and 27 September at 6:00 UTC are shown in Figures 10a and 10b. Figures 10c–10e show the wave height response to currents, while Figures 10f–10h show the corresponding current fields.

the link revealed here between current and wave height variability may be a powerful way to diagnose the current variability at scales not accessible from sea level measurements.

Appendix A: Evaluation of Wind Resolution Effects

We have focused on the effects of currents using winds at a relatively coarse resolution. In order to evaluate the potential impact of higher-resolution winds, we have used a higher-resolution atmospheric simulation using ECMWF's Integrated Forecasting System (IFS) using a cubic octahedral grid, as now operational, but with a 5 km resolution. This model was run in forecast mode. This wind field was used to drive our WAVEWATCH III model configuration of Drake Passage. Figure 9 shows the spectra of the wind speed and wave heights. Although the slope of the H_s spectrum is much less steep than in Figure 5, the spectral level is still much lower than with the current forcing. For example, the spectral density at a wavelength of 50 km ($k = 0.02$ cycles per km) is reduced by a factor 40. It is thus unlikely that the atmospheric variability alone can explain a significant fraction of the variability of wave heights at scales of 25–100 km. However, it is well known that the winds are influenced by small-scale ocean temperature and current gradients, which were not included in these IFS runs.

Appendix B: Different Effects of ROMS and MITgcm Currents on Wave Height Gradients

We have run our wave model with the same winds and boundary forcing for September 2014, and applied the September 2011 MITgcm currents, and the September ROMS currents, looking at the 18 September swell event, and a nor'easter on 27 September. Figure 10 shows the corresponding winds, waves heights, and currents. The wave patterns in Figure 10c are broadly comparable to those obtained for the same day with the June ROMS currents in Figure 1a, the main differences are that the Gulf Stream and the northern ring are located further south in the MITgcm simulation, and the currents are weaker and much more variable in their along-stream direction. We also note the importance of tidal currents at entrances of bays, and banded velocity patterns on the shelf in the MITgcm simulation, which are probably associated with tidally generated internal waves.

Differences are more striking on 27 September. First of all, the intense Gulf Stream simulated by ROMS is located in the region of maximum opposing winds. Second, the smooth along-stream structures of the Gulf Stream and filaments are probably helping in focusing wave energy, with a local enhancement of wave heights that exceeds 50%. In the case of the MITgcm currents, the current gradients are not so much associated to localized sharp features.

Acknowledgments

This work was initiated by the SWOT Science Definition Team and SWOT Algorithm Definition Team, and we thank all members for their questions and suggestions. F.A., J.M., B.C., and N.R. are supported by LabexMER via grant ANR-10-LABX-19-01 and CNES under the SWOT preparation program, S.T.G. and C.R. are supported by the SWOT program with NASA grants (NNX13AE85G, NNX16AH67G, and NNX16AO5OH). CNES and Eumetsat also provided the altimeter data used here, in particular the PEACHI Jason 3 retracked data. Further support was provided by ESA under the Globcurrent project, and ANR grant ANR-14-CE01-0012 MIMOSA. All model results in NetCDF format are available at ftp://ftp.ifremer.fr/ifremer/ww3/HINDCAST/OTHER/SWOT/. Many thanks to M. Accensi and the NCEP team for their contribution to the development and maintenance of the WAVEWATCH III model. The manuscript was greatly improved thanks to at least three anonymous reviewers and Miaohua Mao. High-resolution wind fields produced with the ECMWF IFS model were kindly provided by J. Bidlot.

References

Abdalla, S., and L. Cavaleri (2002), Effect of wind variability and variable air density on wave modelling, *J. Geophys. Res.*, *107*(C7), 3080, doi: 10.1029/2000JC000639.

Andrews, D. G., and M. E. McIntyre (1978), On wave action and its relatives, *J. Fluid Mech.*, *89*, 647–664.

Ardhuin, F., T. H. C. Herbers, P. F. Jessen, and W. C. O'Reilly (2003), Swell transformation across the continental shelf. Part II: Validation of a spectral energy balance equation, *J. Phys. Oceanogr.*, *33*, 1940–1953.

Ardhuin, F., L. Marié, N. Rascle, P. Forget, and A. Roland (2009), Observation and estimation of Lagrangian, Stokes and Eulerian currents induced by wind and waves at the sea surface, *J. Phys. Oceanogr.*, *39*(11), 2820–2838.

Ardhuin, F., J. Tournadre, P. Queffelou, and F. Girard-Ardhuin (2011), Observation and parameterization of small icebergs: Drifting breakwaters in the southern ocean, *Ocean Modell.*, *39*, 405–410, doi:10.1016/j.ocemod.2011.03.004.

Ardhuin, F., et al. (2012), Numerical wave modeling in conditions with strong currents: Dissipation, refraction and relative wind, *J. Phys. Oceanogr.*, *42*, 2101–2120, doi:10.13140/RG.2.1.3125.7207.

Badulin, S. I. (2014), A physical model of sea wave period from altimeter data, *J. Geophys. Res. Oceans*, *119*, 856–869, doi:10.1002/2013JC009336.

Bidlot, J. (2005), Use of Mercator surface currents in the ECMWF forecasting system: A follow-up study, *Tech. Rep. Mem. R60.9/JB/1228*, Res. Dep., ECMWF, Reading, U. K.

Bourassa, M. A., E. Rodriguez, and D. Chelton (2016), Winds and current mission: Ability to observe mesoscale air/sea coupling, in *IEEE International Geoscience and Remote Sensing Symposium (IGARSS)*, pp. 7392–7395, IEEE, Washington, D. C., doi:10.1109/IGARSS.2016.7730928.

Callies, J., R. Ferrari, J. M. Klymak, and J. Gula (2015), Seasonality in submesoscale turbulence, *Nat. Commun.*, *6*, 6862, doi:10.1038/ncomms7862.

Capet, X., J. C. Mcwilliams, M. J. Molemaker, and A. F. Shchepetkin (2016), Mesoscale to submesoscale transition in the California current system. Part i: Flow structure, eddy flux, and observational test, *J. Phys. Oceanogr.*, *38*, 29–43, doi:10.1175/2007JPO3671.

Cardone, V. J., R. E. Jensen, D. T. Resio, V. R. Swail, and A. T. Cox (1996), Evaluation of contemporary ocean wave models in rare extreme events: The "halloween storm" of October 1991 and the storm of the century of March 1993, *J. Atmos. Oceanic Technol.*, *13*(1), 198–230.

Chapron, B., F. Collard, and F. Ardhuin (2005), Direct measurements of ocean surface velocity from space: Interpretation and validation, *J. Geophys. Res.*, *110*, C07008, doi:10.1029/2004JC002809.
Chelton, D. B., M. G. Schlax, M. H. Freilich, and R. F. Milliff (2004), Satellite measurements reveal persistent small-scale features in ocean winds, *Science*, *303*, 978–983.
Collard, F., A. Mouche, B. Chapron, C. Danilo, and J. Johannessen (2008), Routine high resolution observation of selected major surface currents from space, in *Proceedings of SEASAR 2008, SP-656*, ESA-ESRIN, Frascati, Italy.
Dibarboure, G., F. Boy, J. D. Desjonqueres, S. Labroue, Y. Lasne, N. Picot, J. C. Poisson, and P. Thibaut (2014), Investigating short-wavelength correlated errors on low-resolution mode altimetry, *J. Atmos. Oceanic Technol.*, *31*, 1337–1362, doi:10.1175/JTECH-D-13-00081.1.
Dong, S., J. Sprintall, and S. T. Gille (2006), Location of the Antarctic polar front from AMSR-E satellite sea surface temperature measurements, *J. Phys. Oceanogr.*, *36*, 2075–2089.
Durand, M., L.-L. Fu, D. Lettenmaier, D. Alsdorf, E. Rodriguez, and D. Esteban-Fernandez (2010), The surface water and ocean topography mission: Observing terrestrial surface water and oceanic submesoscale eddies, *Proc. IEEE*, *98*(5), 766–779.
Gallet, B., and W. R. Young (2014), Refraction of swell by surface currents, *J. Mar. Res.*, *72*, 105–126.
Gula, J., M. J. Molemaker, and J. C. Mcwilliams (2015), Gulf Stream dynamics along the southeastern U.S. seaboard, *J. Phys. Oceanogr.*, *45*, 690–715.
Gutshabash, Y. S., and I. V. Lavrenov (1986), Swell transformation in the cape Agulhas current, *Izv. Atmos. Oceanic Phys.*, *22*(6), 494–497.
Hall, T. M., and A. H. Sobel (2013), On the impact angle of hurricane Sandy's New Jersey landfall, *Geophys. Res. Lett.*, *40*, 2312–2315, doi:10.1002/grl.50395.
Herbers, T. H. C., E. J. Hendrickson, and W. C. O'Reilly (2000), Propagation of swell across a wide continental shelf, *J. Geophys. Res.*, *105*(C8), 19,729–19,737.
Hersbach, H., and J. R. Bidlot (2008), The relevance of ocean surface current in the ECMWF analysis and forecast system, in *Proceedings From the ECMWF Workshop on Atmosphere-Ocean Interaction*, ASCE, Reading, U. K.
Holthuijsen, L. H., and H. L. Tolman (1991), Effects of the Gulf Stream on ocean waves, *J. Geophys. Res.*, *96*(C7), 12,755–12,771.
Irvine, D. E., and D. G. Tilley (1988), Ocean wave directional spectra and wave-current interaction in the Agulhas from the shuttle imaging radar-B synthetic aperture radar, *J. Geophys. Res.*, *93*(C12), 15,389–15,401.
Kirby, J. T., and T.-M. Chen (1989), Surface waves on vertically sheared flows: Approximate dispersion relations, *J. Geophys. Res.*, *94*(C1), 1013–1027.
Klein, P., and G. Lapeyre (2009), The oceanic vertical pump induced by mesoscale and submesoscale turbulence, *Annu. Rev. Mar. Sci.*, *1*, 351–375.
Komen, G. J., L. Cavaleri, M. Donelan, K. Hasselmann, S. Hasselmann, and P. A. E. M. Janssen (1994), *Dynamics and Modelling of Ocean Waves*, 554 pp., Cambridge Univ. Press, Cambridge, U. K.
Kudryavtsev, V., D. Akimov, J. Johannessen, and B. Chapron (2005), On radar imaging of current features: 1. Model and comparison with observations, *J. Geophys. Res.*, *110*, C07016, doi:10.1029/2004JC002505.
Kudryavtsev, V., A. Myasoedov, B. Chapron, J. A. Johannessen, and F. Collard (2012), Imaging mesoscale upper ocean dynamics using synthetic aperture radar and optical data, *J. Geophys. Res.*, *117*, C04029, doi:10.1029/2011JC007492.
Kudryavtsev, V., P. Golubkin, and B. Chapron (2015), A simplified wave enhancement criterion for moving extreme events, *J. Geophys. Res. Oceans*, *120*, 7538–7558, doi:10.1002/2015JC011284.
Kudryavtsev, V., M. Yurovskaya, B. Chapron, F. Collard, and C. Donlon (2017), Sun glitter imagery of surface waves: 2. Waves transformation on ocean currents, *J. Geophys. Res. Oceans*, *122*, 1384–1399, doi:10.1002/2016JC012426.
Longuet-Higgins, M. S. (1963), The effect of non-linearities on statistical distributions in the theory of sea waves, *J. Fluid Mech.*, *17*, 459–480.
Magne, R., K. Belibassakis, T. H. C. Herbers, F. Ardhuin, W. C. O'Reilly, and V. Rey (2007), Evolution of surface gravity waves over a submarine canyon, *J. Geophys. Res.*, *112*, C01002, doi:10.1029/2005JC003035.
Mapp, G. R., C. S. Welch, and J. C. Munday (1985), Wave refraction by warm core rings, *J. Geophys. Res.*, *90*(C4), 7153–7162.
McWilliams, J. C. (2016), Submesoscale currents in the ocean, *Proc. R. Soc. A*, *427*, 1–32, doi:10.1098/rspa.2016.0117.
Melville, W. K., F. C. Felizardo, and P. Matusov (2004), Wave slope and wave age effects in measurements of electromagnetic bias, *J. Geophys. Res.*, *109*, C07018, doi:10.1029/2002JC001708.
Mori, N. (2012), Freak waves under typhoon conditions, *J. Geophys. Res.*, *117*, C00J07, doi:10.1029/2011JC007788.
Munk, W., L. Armi, K. Fischer, and F. Zachariasen (2000), Spirals on the sea, *Philos. Trans. R. Soc. London A*, *456*, 1217–1280.
Osborne, A. R., and T. L. Burch (1980), Coupling between a surface-wave spectrum and an internal wave: Modulation interaction, *Science*, *208*(4443), 513–460.
Penven, P., I. Halo, S. Pous, and L. Marié (2014), Cyclogeostrophic balance in the Mozambique Channel, *J. Geophys. Res. Oceans*, *119*, 1054–1067, doi:10.1002/2013JC009528.
Peral, E., E. Rodriguez, and D. Esteban-Fernandez (2015), Impact of surface waves on SWOT's projected ocean accuracy, *Remote Sens.*, *7*(11), 14,509–14,529, doi:10.3390/rs71114509.
Phillips, O. M. (1984), On the response of short ocean wave components at a fixed wavenumber to ocean current variations, *J. Phys. Oceanogr.*, *14*, 1425–1433.
Rascle, N., and F. Ardhuin (2009), Drift and mixing under the ocean surface revisited stratified conditions and model-data comparisons, *J. Geophys. Res.*, *114*, C02016, doi:10.1029/2007JC004466.
Rascle, N., and F. Ardhuin (2013), A global wave parameter database for geophysical applications. part 2: Model validation with improved source term parameterization, *Ocean Modell.*, *70*, 174–188, doi:10.1016/j.ocemod.2012.12.001.
Rascle, N., B. Chapron, A. Ponte, F. Ardhuin, and P. Klein (2014), Surface roughness imaging of currents shows divergence and strain in the wind direction, *J. Phys. Oceanogr.*, *44*, 2153–2163, doi:10.1175/JPO-D-13-0278.1.
Rio, M.-H., S. Mulet, and N. Picot (2014), Beyond GOCE for the ocean circulation estimate: Synergetic use of altimetry, gravimetry, and in situ data provides new insight into geostrophic and Ekman currents, *Geophys. Res. Lett.*, *41*, 8918–8925, doi:10.1002/2014GL061773.
Rocha, C. B., T. K. Chereskin, and S. T. Gille (2016), Mesoscale to submesoscale wavenumber spectra in Drake passage, *J. Phys. Oceanogr.*, *46*, 601–620, doi:10.1175/JPO-D-15-0087.1.
Roland, A., and F. Ardhuin (2014), On the developments of spectral wave models: Numerics and parameterizations for the coastal ocean, *Ocean Dyn.*, *64*(6), 833–846.
Romero, L., L. Lenain, and W. K. Melville (2017), Observations of surface-wave-current interaction, *J. Phys. Oceanogr.*, doi:10.1175/JPO-D-16-0108.1, in press.
Rouault, M. J., A. Mouche, F. Collard, J. A. Johannessen, and B. Chapron (2010), Mapping the Agulhas Current from space: An assessment of ASAR surface current velocities, *J. Geophys. Res.*, *115*, C10026, doi:10.1029/2009JC006050.

Sandwell, D. T., and W. H. F. Smith (2005), Retracking ERS-1 altimeter waveforms for optimal gravity field recovery, *Geophys. J. Int.*, *163*, 79–89, doi:10.1111/j.1365-246X.2005.02724.x.

Sasaki, H., P. Klein, B. Qiu, and Y. Sasai (2014), Impact of oceanic-scale interactions on the seasonal modulation of ocean dynamics by the atmosphere, *Nat. Commun.*, *5*, 5636, doi:10.1038/ncomms6636.

Sepulveda, H. H., P. Queffeulou, and F. Ardhuin (2015), Assessment of SARAL AltiKa wave height measurements relative to buoy, Jason-2 and Cryosat-2 data, *Mar. Geod.*, *38*(S1), 449–465, doi:10.1080/01490419.2014.1000470.

Shcherbina, A. Y., et al. (2015), The LATMIX summer campaign, submesoscale stirring in the upper ocean, *Bull. Am. Meteorol. Soc.*, *96*(8), 1257–1279.

Srokosz, M. A. (1986), On the joint distribution of surface elevation and slopes for a nonlinear random sea, with an application to radar altimetry, *J. Geophys. Res.*, *91*(C1), 995–1006.

Suzuki, N., B. Fox-Kemper, P. E. Hamlington, and L. P. van Roekel (2016), Surface waves affect frontogenesis, *Geophys. Res. Lett.*, *121*, 3597–3624, doi:10.1002/2015JC011563.

SKIM Team (2016), Sea surface kinematics multiscale monitoring: Full proposal for ESA Earth Explorer 9, 66 pp., ResearchGate GmbH, Berlin Germany, doi:10.13140/RG.2.1.3125.7207.

Tolman, H. L. (1990), The influence of unsteady depths and currents of tides on wind-wave propagation in shelf seas, *J. Phys. Oceanogr.*, *20*, 1166–1174.

Tolman, H. L. (2003), Treatment of unresolved islands and ice in wind wave models, *Ocean Modell.*, *5*, 219–231.

Tran, N., D. Vandemark, S. Labroue, H. Feng, B. Chapron, H. L. Tolman, J. Lambin, and N. Picot (2010), The sea state bias in altimeter sea level estimates determined by combining wave model and satellite data, *J. Geophys. Res.*, *115*, C03020, doi:10.1029/2009JC005534.

Valladeau, G., P. Thibaut, B. Picard, J. C. Poisson, N. Tran, N. Picot, and A. Guillot (2015), Using SARAL/AltiKa to improve Ka-band altimeter measurements for coastal zones, hydrology and ice: The PEACHI prototype, *Mar. Geod.*, *38*, suppl. 1, 124–142, doi:10.1080/01490419.2015.1020176.

Vandemark, D., B. Chapron, T. Elfouhaily, and J. W. Campbell (2005), Impact of high-frequency waves on the ocean altimeter range bias, *J. Geophys. Res.*, *110*, C11006, doi:10.1029/2005JC002979.

Waseda, T., M. Hallerstig, K. Ozaki, and H. Tomita (2011), Enhanced freak wave occurrence with narrow directional spectrum in the North Sea, *Geophys. Res. Lett.*, *38*, L13605, doi:10.1029/2011GL047779.

White, B. S. (1999), Wave action on currents with vorticity, *J. Fluid Mech.*, *386*, 329–344.

White, B. S., and B. Fornberg (1998), On the chance of freak waves at sea, *J. Fluid Mech.*, *355*, 113–138.

WAVEWATCH III Development Group (2016), User manual and system documentation of WAVEWATCH III version 5.16, *Tech. Note 329*, 326 pp., NOAA/NWS/NCEP/MMAB, College Park, Md.

WISE Group (2007), Wave modelling—The state of the art, *Prog. Oceanogr.*, *75*, 603–674, doi:10.1016/j.pocean.2007.05.005.